Rev. Roum. Sci. Techn.– Électrotechn. et Énerg.
Vol. **71**, *4*, pp. 489–494, Bucarest, 2026

GRID-FORMING VIRTUAL SYNCHRONOUS GENERATOR CONTROL FOR CASCADED H-BRIDGE MULTILEVEL INVERTER

SABRINA NACEF[1*], BESSAM AMROUCHE[1], RABAH BABOURI[1], KACI GHEDAMSI[1]

Keywords: Virtual synchronous generator (VSG); Grid-forming inverter; Cascaded H-bridge multilevel inverter (CHB-MLI); Voltage-droop control; Photovoltaic (PV) integration; Power quality.

This paper presents a modeling and control framework for a 10 MVA, 6.6 kV photovoltaic-fed cascaded H-bridge multilevel inverter (CHB-MLI) in weak-grid applications. To counter reduced stability and missing inertia from high renewable penetration, grid-forming inverters with Virtual Synchronous Generator (VSG) control emulate synchronous machines by providing synthetic inertia and damping, while the multilevel topology enhances power quality through reduced harmonic distortion and extended voltage capability. Simulation results confirm excellent dynamic performance during load increases and seamless islanding transitions, keeping grid current and voltage THD well within IEEE 519 standards.

1. INTRODUCTION

In recent years, renewable energy sources (RES) have expanded rapidly to address climate change and reduce greenhouse gas emissions. Solar photovoltaic (PV) systems, in particular, have seen remarkable growth, with global capacity surpassing 800 GW in 2020 [1]. Despite this progress, integrating intermittent RES into existing grids remains challenging. Traditional power systems, built around centralized synchronous generators (SGs), inherently provide inertia, voltage regulation, and frequency stability [2]. These machines are directly coupled to the grid, where their mechanical inertia helps damp frequency fluctuations and supports overall system stability [3].

The growing penetration of inverter-based renewables is disrupting traditional power system operation. Unlike synchronous generators (SGs), most renewables lack physical inertia and intrinsic frequency control [3], leading to reduced system resilience and weaker voltage and reactive power support, especially in weak grids [1]. To address this, grid-forming inverters have emerged as a key solution. Beyond converting PV-generated DC into AC, they actively establish grid voltage and frequency, ensuring stability in weak or islanded networks. A prominent approach is the virtual synchronous generator, which emulates SG behavior by introducing synthetic inertia and damping, thereby enhancing frequency and voltage stability in low-inertia systems [4].

Grid-forming inverters have progressed notably over recent decades. Initial two-level designs, though effective, suffered from limits in efficiency, harmonic distortion, and voltage levels. To address these issues, multilevel inverters (MLIs) emerged, offering reduced THD, higher voltage capability, and better efficiency. Their ability to generate smoother waveforms makes them well-suited for renewable energy integration [5]. Among them, cascaded H-bridge MLIs are widely adopted due to their modularity and scalability, enabling the connection of multiple PV sources with high performance. Research has focused on improving their control strategies for power quality, fault tolerance, and dynamic response [6,7]. More recent studies emphasize intelligent methods, including fuzzy logic and hybrid controls, for handling renewable systems under grid fluctuations [8,9].

With rising RES penetration, grid-forming control is essential. Virtual synchronous generators (VSGs) stand out by providing inertia, frequency regulation, and voltage support. Through the virtual swing equation and rotor angle, they generate voltage and frequency dynamically, ensuring stability and autonomous operation in weak grids [10]. Unlike grid-following inverters that depend on PLLs, VSGs establish their own reference frame via the evolving virtual rotor angle, which is used in the Park transformation for synchronized voltage and current control [11].

Recent research has demonstrated the effectiveness of VSGs in various applications, particularly in microgrids and isolated systems. In [12], the authors showed that VSGs improve frequency and voltage stability under low short-circuit capacity and high grid impedance. Other works have examined enhancements to the basic VSG concept, such as adaptive inertia tuning [13], frequency deviation feedforward [14], and voltage-current hybrid control [15].

Integrating energy storage systems with VSGs has also been explored to mitigate the effects of power fluctuations and maintain power balance under varying load conditions [16]. Additionally, VSGs have been employed for fault ride-through, system re-synchronization, and coordinated microgrid islanding strategies [17].

A major research gap remains in assessing grid-forming VSG performance integrated with modular CHB topologies in weak grids. Existing literature relies on stiff DC sources and two-level converters, neglecting coupled dynamics and multivariable non-linear interactions between decentralized DC-link voltage stability, PV fluctuations, virtual inertia emulation, and grid impedance variations.

To address this, we propose a modeling and control framework for a PV-based CHB multilevel inverter targeting weak grids where conventional grid-following control fails. Key contributions include full VSG control modeling—incorporating the virtual swing equation, voltage droop control, and Park transformation using the virtual rotor angle—paired with a Thévenin equivalent circuit to analyze dynamic grid interactions.

The remainder of this paper is structured as follows: Section 2 introduces the modeling of the PV-based cascaded H-bridge inverter, the DC-link, the LC filter, and the weak grid. Section 3 explains the grid-forming VSG control with its hierarchical loops. Section 4 presents the simulation results, highlighting system performance and stability. Finally, Section 5 concludes the work and outlines future research directions.

2. SYSTEM MODELLING

Figure 1 shows the overall system, which includes a

[1] Université de Béjaïa, Faculté de Technologie, Laboratoire de Maîtrise des Énergies Renouvelables, 06000 Béjaïa, Algérie.
E-mail: sabrina.nacef@univ-bejaia.dz, bessam.amrouche@univ-bejaia.dz, rabah.babouri@univ-bejaia.dz,kaci.ghedamsi@univ-bejaia.dz.

DOI: 10.59277/RRST-EE.2026.4.2

cascaded half-bridge inverter where each submodule is connected to a PV source through a DC-link capacitor. The PVs are modeled as identical constant DC sources to simplify DC-side dynamics. The inverter feeds a weak grid modeled by an ideal voltage source in series with impedance and supplies an active load. A LC filter with $L_{in}$and C is added to suppress harmonics and smooth grid integration. Control is organized hierarchically with an inner current loop, a voltage loop, and an outer VSG loop, ensuring power regulation and emulation of synchronous machine dynamics at the PCC. Detailed modeling of subsystems and controls is given in the next sections.

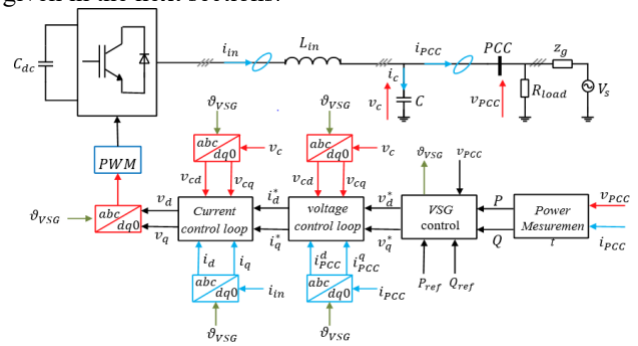

Fig. 1 – System globally studied.

2.1 INVERTER MODELLING

The cascaded H-bridge inverter topology and switching behavior were presented in [18]. In this work, the same structure is used, with each phase composed of N cascaded sub-modules (SMs), each containing a half-bridge, a DC capacitor, and two IGBTs. Modulation controls the number of inserted SMs per arm via the insertion index $n \in [0,1]$. The instantaneous output voltage for phase $j \in \{a,b,c\}$ is expressed as:

$$v_{in,j} = n.\sum_{1}^{N} v_{dc,j}. \quad (1)$$

where $\sum_1^N v_{dc}$is the total voltage of all capacitors in phase j. The inverter is supplied by a PV source, and the relation between the PV current $i_{PV,j}$, the inverter output current $i_{in,f}$, and the capacitor current $i_{dc,j}$ is

$$i_{PV,j}=i_{in,j}+i_{dc,j}, \quad (2)$$

with

$$i_{dc,j} = C_{dc,j}\frac{\mathrm{d}\left(\sum_1^N v_{dc,j}\right)}{\mathrm{d}t}. \quad (3)$$

Substituting into the current balance yields the inverter current:

$$i_{in,j}=i_{PV,j} - C_{dc,j}\frac{\mathrm{d}\left(\sum_1^N v_{dc,j}\right)}{\mathrm{d}t}. \quad (4)$$

The inverter is connected to the grid through an LC filter. Applying Kirchhoff's voltage law at the filter output gives:

$$\frac{\mathrm{d}i_{in,j}}{\mathrm{d}t} = -\frac{R_{in}}{L_{in}}i_{in,j} + \frac{n}{L_{in}}\sum_{1}^{N} v_{dc,j} - \frac{V_{c,j}}{L_{in}}. \quad (5)$$

The overall continuous-time model for a single phase j of the inverter can thus be expressed in a compact state-space form:

$$\begin{bmatrix} \frac{\mathrm{d}i_{in,j}}{\mathrm{d}t} \\ \frac{\mathrm{d}\left(\sum_1^N v_{dc,j}\right)}{\mathrm{d}t} \end{bmatrix} = \begin{bmatrix} -\frac{R_{in}}{L_{in}} & \frac{n}{L_{in}} \\ -\frac{1}{\mathrm{C_{dc,j}}} & 0 \end{bmatrix} \begin{bmatrix} i_{in,j} \\ \sum_1^N v_{dc,j} \end{bmatrix} + \begin{bmatrix} -\frac{V_{c,j}}{L_{in}} \\ \frac{\mathrm{i_{PV,j}}}{\mathrm{C_{dc,j}}} \end{bmatrix}. \quad (6)$$

This model captures the coupling between the power sources (PV), the inverter, and the DC-link capacitor dynamics. It will serve as the foundation for the control system design in the next sections.

2.2 LC FILTER MODELLING

In this section, we describe the design of the LC filter (Fig. 2) for a grid-connected inverter system; the model used in this paper was derived from [19].

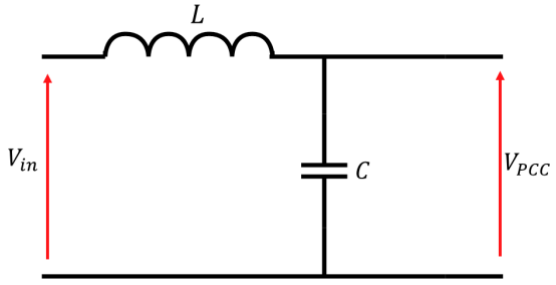

Fig. 2 – LC filter model

The key parameters are described in Table 1.

Table 1

Key parameters for LC filter design.

Parameter	Value
Rated Power S_n	10 MVA
Grid Voltage (Line-to-Line) U_n	6.6 kV
DC Link Voltage V_{dc}	1700 V
Grid Frequency f_n	50 Hz
Switching Frequency f_{sw}	10 kHz

The first step in filter design is selecting the inverter-side inductance to limit current ripple to about 10% of the nominal value. The inductance L_{in} is then calculated from the maximum ripple and switching frequency:

$$L_{in} = \frac{V_{dc}}{16 f_{sw} \Delta I_{L-max}}, \quad (7)$$

where the maximum current ripple is

$$\Delta I_{L-max} = 0.1\frac{S_n\sqrt{2}}{U_n}. \quad (8)$$

For the capacitance, we limit it to 5% of the base capacitance C_b to maintain the size and cost:

$$C = 0.05 \times C_b. \quad (9)$$

The base capacitance C_b, which depends on the grid frequency f_n and the base impedance, Z_b, is given by:

$$C_b = \frac{1}{2\pi f_n \times Z_b}, \quad (10)$$

where the base impedance Z_b, which relates the rated power S_n to the grid voltage U_n at the phase level is:

$$Z_b = U_n^2/S_n. \quad (11)$$

2.3 RESONANT FREQUENCY

The final step in filter design is to set the resonant frequency properly. It should be higher than the grid frequency to avoid interaction with the fundamental, and lower than half the switching frequency to attenuate switching harmonics. For an LC filter, the resonant frequency is given by:

$$f_{res} = \frac{1}{2\pi\sqrt{LC}}. \quad (12)$$

Table 2 shows the LC filter design summary per phase, where each shows effective harmonic attenuation beyond the switching frequency. The inductance and capacitance values offer a good balance between size, cost, and performance.

Table 2
Filter designed parameters

Parameter	Value
Inductance L_{in}	25.2 mH
Capacitance C	10.95 µF
Resonant Frequency f_{res}	307 Hz

2.4 GRID AND LOAD MODELLING

The grid is represented by a Thevenin equivalent circuit, a standard method for weak grids. Such grids are characterized by high source impedance, low short-circuit capacity, and strong sensitivity to power disturbances [20]. The model includes an ideal voltage source V_s in series with grid impedance Z_g, and a resistive load connected at the PCC, as shown in Fig. 3.

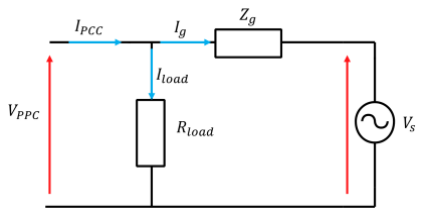

Fig. 3 – Weak grid model.

The governing equation at the PCC is derived from Kirchhoff's voltage Law:

$$V_s = V_{PPC} + Z_g I_g, \tag{13}$$

where the grid impedance can be represented in eq. (14) as:

$$Z_g = R_g + \mathrm{j}\omega_g L_g, \tag{14}$$

where R_g and L_g: the resistance and inductance of the grid, respectively.

The source voltage is given by

$$V_s = V_M \sin(\omega t), \tag{15}$$

and since the load is a pure resistance, we have

$$I_{load} = \frac{V_{PPC}}{R_{load}}. \tag{16}$$

Using current sharing at the PCC we will have

$$I_g = I_{PCC} - I_{load}. \tag{17}$$

Replacing eq. (16) and eq. (17) in eq. (13), we find

$$V_{PPC} = V_s - \left(R_g + \mathrm{j}\omega_g L_g\right)\left(I_{PCC} - \frac{V_{PPC}}{R_{load}}\right), \tag{18}$$

where V_{PPC} is the voltage at the PCC, I_g the current injected into the grid, ω_g the grid angular frequency, I_{load} the load current, R_{load} the load resistance, and I_{PCC} the current at the PCC.

To have an accurate weak grid model, the impedance parameters R_g and L_g must be selected such that they reflect realistic grid conditions. These parameters are derived based on the grid short-circuit power (S_{sc}) at the PCC. The following equation outlines how to calculate them, where $\emptyset$ is the angle between grid voltage and grid current,

$$|Z_g| = \frac{V_{PPC}^2}{S_{sc}}, \tag{19}$$

$$R_g = |Z_g|\cos(\emptyset),\ L_g = \frac{|Z_g|\sin(\emptyset)}{\omega_g}. \tag{20}$$

The angle between voltage and current is typically small in strong grids, larger in weak grids,

3. INVERTER VOLTAGE AND CURRENT REGULATION

The voltage and current control loops used are shown in Fig. 4. The inner current loop is used to regulate the output current of the inverter; the inner references are obtained from the outer voltage loop used to maintain adequate voltage references for the CHB-MLIs, and it controls the output voltage of the capacitor filter used [21].

The inner current loop outputs are then used as a voltage reference to the pulse width modulation (PWM) control after an inverse Clark and Park transformation.

4. VIRTUAL SYNCHRONOUS GENERATOR CONTROL

To enable grid-forming operation, the inverter is controlled as a VSG. The proposed control strategy, illustrated in Fig. 5, reproduces the dynamic behavior of a conventional synchronous machine by introducing virtual inertia and emulating frequency and voltage droop responses. Its objective is to enhance system stability and provide auxiliary services such as frequency and voltage regulation, especially under weak-grid conditions.

4.1 FREQUENCY CONTROL

The frequency control strategy is used to enable grid-forming operation of the voltage source converter (VSC) by emulating the dynamics of a synchronous generator. Unlike grid-following systems, a grid-forming VSG establishes the grid voltage and frequency at the PCC, making it suitable for weak or isolated grids. The VSC is controlled through a virtual synchronous generator model that introduces virtual inertia, allowing autonomous frequency and phase definition while improving stability and dynamic response.

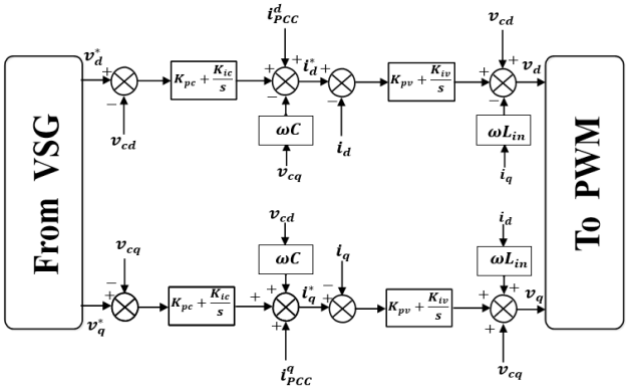

Fig. 4 – Voltage and current control.

The virtual frequency dynamics ω_{VSG} are governed by the following swing equation:

$$\begin{cases} J\dfrac{\mathrm{d}\omega_{VSG}}{\mathrm{d}t} = \dfrac{P_m}{\omega_{ref}} - \dfrac{P_{mes}}{\omega_{ref}} - K_D(\omega_{VSG} - \omega_{pcc}), \\ \vartheta_{VSG} = \dfrac{\mathrm{d}\omega_{VSG}}{\mathrm{d}t}, \end{cases} \tag{21}$$

where J is the virtual inertia constant, P_m the virtual mechanical power input, P_{mes} the measured output power, ω_{ref} the nominal system frequency, K_D the damping coefficient, and ϑ_{VSG} the virtual rotor angle. The input power is defined as:

$$P_m = P_{ref} + \frac{1}{D_p}(\omega_{ref} - \omega_{pcc}), \tag{22}$$

where P_{ref} is the active power reference and D_p is the frequency droop coefficient. This formulation enables the VSG to replicate both inertial and droop-based responses, ensuring stable frequency regulation.

Moreover, ϑ_{VSG} is used in the Park transformation,

aligning the control reference frame with the VSG rotating frame for accurate voltage and current regulation.

The virtual inertia constant J was tuned via $J = \frac{2HS_n}{\omega_0^2}$ to limit the maximum frequency deviation ($\Delta f_{\max}$) while maintaining a fast-settling time without transient overshoots

4.2 VOLTAGE CONTROL

The voltage droop control is designed to mimic the Q–V characteristic of a synchronous machine by adjusting the reference voltage according to reactive power deviation, as given by:

$$v_d^* = v_{PCC} + \frac{1}{D_q}(Q_{ref} - Q_{mes}), \quad (23)$$

where v_d^* is the d-axis voltage reference, v_{ppc} the measured PCC voltage, Q_{ref} the reactive power reference, Q_{mes} the measured reactive power, and D_q the voltage droop coefficient. This ensures a linear relation between voltage adjustment and reactive power.

In the synchronous frame, v_d^* serves as the d-axis reference, while the q-axis reference is set to:

$$v_q^* = 0. \quad (24)$$

This configuration decouples active and reactive power control, with active power regulated via the d-axis and reactive power via voltage magnitude. The references (v_d^*, v_q^*) feed the outer voltage loop, which generates current references for the inner current loop. The final outputs drive the PWM modulator, producing the inverter switching signals.

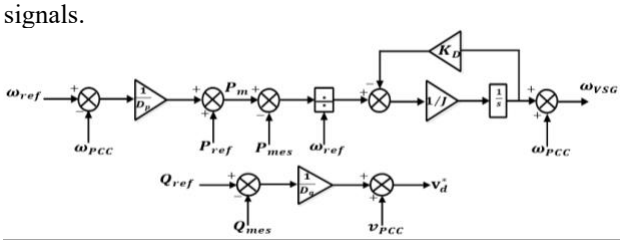

Fig. 5– VSG control.

5. SIMULATIONS AND RESULTS

To evaluate the grid-forming capability of the proposed VSG-controlled 7-level CHB inverter in weak-grid conditions, time-domain simulations were conducted using the parameters in Table 3.

Table 3

Simulation parameters

Parameters	values
Grid parameters	
Phase-to-phase grid voltage V_{ph-ph}	6.6 kv
Grid frequency f_g	50 Hz
Three phase short circuit level at base voltage for weak grid	20MVA
X/R ratio	7
Load parameters	
Local load	5.445 Ω
additional load	3.355 Ω
VSG parameters	
Virtual inertia J	166.67 kg.m^2
Damping coefficient K_D	10^6Nms/rad
Active droop control D_p	500
Reactive droop control D_q	10^{-5}
the nominal system frequency ω_{ref}	2π50 rad/s
the active power reference P_{ref}	10 MW
The reactive power reference Q_{ref}	0 VAR

The test sequence examines transient dynamics under a 60% active load step ($t = 1.0$ s) followed by an islanding transition ($t = 2.0$ s).

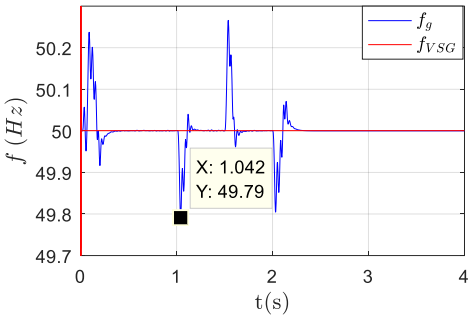

Fig. 6 – Grid and VSG frequency dynamics under load increase and islanding events.

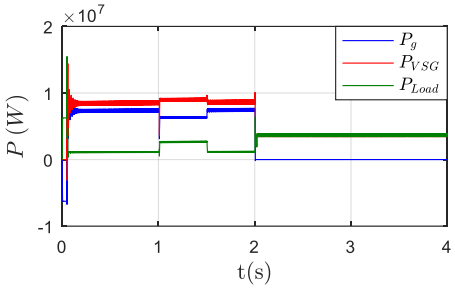

Fig. 7– Active power sharing between grid, VSG, and load under load increase and islanding events.

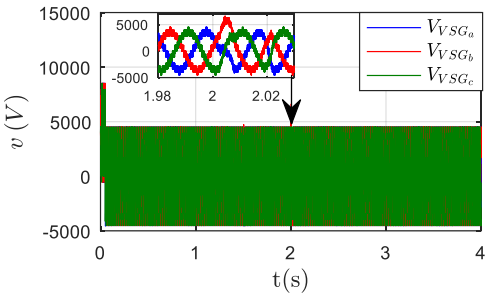

Fig. 8 – Inverter output voltage.

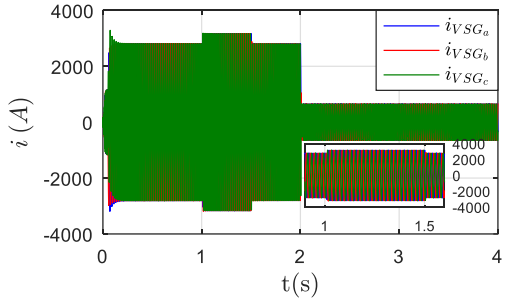

Fig. 9 – Inverter output current.

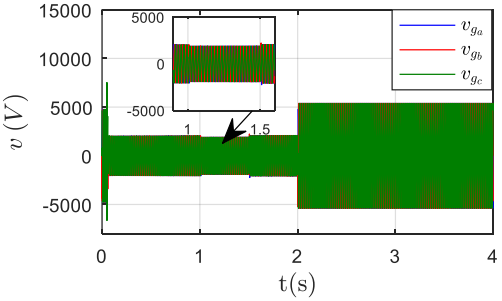

Fig. 10 – Grid voltage.

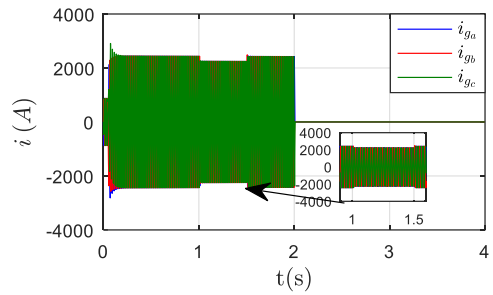

Fig. 11 – Grid current.

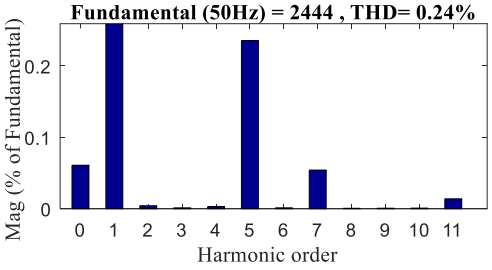

Fig. 12– Harmonic spectrum of the grid current at t = 0.7 s.

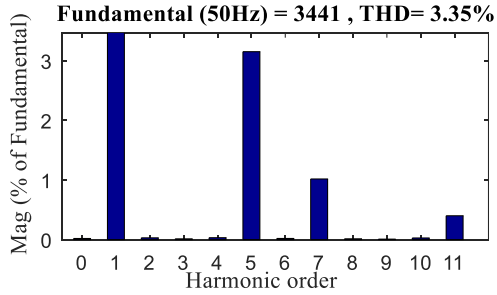

Fig. 13 – Harmonic spectrum of the grid voltage at t =0.7 s.

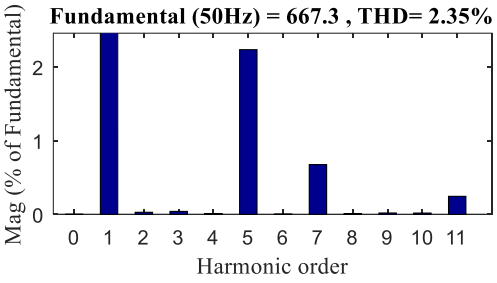

Fig. 14 – Harmonic spectrum of the load current at t = 2.5 s.

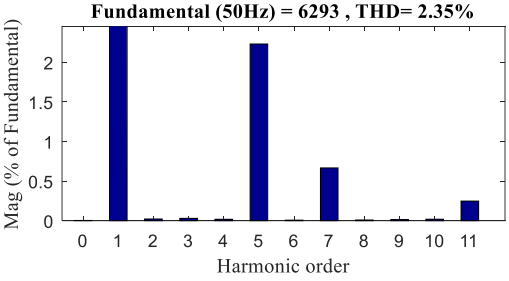

Fig. 15– Harmonic spectrum of the load voltage at t = 2.5 s.

5.1 DYNAMIC PERFORMANCE ANALYSIS

Active load step ($t = 1.0$ s): an abrupt 60% active load step triggers a transient frequency disturbance. Emulated virtual inertia absorbs the kinetic power deficit, dampening the rate of change of frequency (RoCoF) and limiting the frequency nadir to $f_{\min} = 49.79$ Hz ($\Delta f_{\max} = 0.21$ Hz) with a rapid settling time of $t_s = 0.25$ s (Fig. 6). Simultaneously, active power generation scales up to match load demand without loss of synchronism (Fig. 7). This power ramp is mirrored by a swift, well-damped increase in inverter output current without overcurrent spikes (Fig. 9), while grid PCC voltage experiences negligible steady-state degradation (Fig. 10).

Islanding Transition ($t = 2.0$ s): Disconnecting the grid breaker causes grid voltage and current to collapse cleanly to zero (Fig. 10, Fig. 11). The inverter autonomously establishes the local grid reference frame, shifting seamlessly to islanded mode to supply the active loads (Fig. 7). Inverter output current smoothly adjusts to carry the full isolated load current (Fig. 9). Due to the virtual droop mechanism, output line voltage undergoes a minor transient sag of $\Delta V = 2.1\%$, recovering to steady-state within $t_{\text{rec}} = 0.18$ s (Fig. 8).

5.2 POWER QUALITY AND HARMONIC EVALUATION

Harmonic performance was evaluated during steady-state grid-connected and islanded conditions. All parameters strictly comply with IEEE 519 standard limits (THD $< 5\%$):

Table 4

Total harmonic distortion compliance across operating regimes.

Operating Regime	Signal	THD (%)
Grid-Connected	Grid Current	0.24%
Grid-Connected	Grid Voltage	3.31%
Islanded	Load Current	2.35%
Islanded	Load Voltage	2.35%

These quantitative findings demonstrate that integrating synthetic inertia with voltage-droop control effectively dampens frequency transients, mitigates voltage sags, and maintains current regulation during severe grid decoupling events while preserving low harmonic content

6. **CONCLUSION**

This paper presented a grid-forming Virtual Synchronous Generator control framework for a 10 MVA cascaded H-bridge multilevel inverter operating in weak grids. By synthesizing virtual inertia and voltage-droop mechanisms, the proposed control achieves stable PLL-free regulation, fast damping during load transients, and seamless islanding transitions. The findings demonstrate that pairing VSG control with modular CHB topologies provides a reliable, scalable solution to low-inertia instability in renewable-dominated power systems. While this study assumes resistive loading and constant grid impedance, future work will address non-linear loads, integrate submodule fault-tolerant control, and validate system dynamics via Hardware-in-the-Loop (HIL) testing.

CREDIT AUTHORSHIP CONTRIBUTION STATEMENT

Sabrina NACEF: Conducted the literature review, developed the program, organized the manuscript, and wrote the original draft.

Bessam AMROUCHE: Proofread the manuscript and edited it to enhance clarity, precision, and coherence.

Rabah BABOURI: Proofread the text to improve readability, rigor, and flow.

Kaci GHEDAMSI: Validated the results and findings, contributed to document organization, and proofread the text to improve readability, rigor, and flow.

Received on 9 September 2025

REFERENCES

1. ***IEA, "Renewable energy market update," International Energy Agency (2021).
2. F. Shahnazian, K. Das, R. Yan, P. Sørensen, "Challenges of renewable energy integration to weak grids," IET Conf. Proc. (2023).
3. X. Gao, D. Zhou, A. Anvari-Moghaddam, F. Blaabjerg, "Stability analysis of grid-following and grid-forming converters based on state-space modelling," IEEE Trans. Ind. Appl., **60**, *3*, pp. 4910–4920 (2024).
4. S. Kouro et al., "Recent advances and industrial applications of multilevel converters," IEEE Trans. Ind. Electron., **57**, *8*, pp. 2553–2580 (2010).
5. A.F. Kasse, N. Kabeche, S. Moulahoum, "Separate integration of solar PVs into the low-voltage DC link of a solid-state transformer based on a modular multilevel converter," Rev. Roum. Sci. Techn. – Électrotechn. Et Énerg., **70**, *1*, pp. 33–38 (2025).
6. M.M. Adnan, A. Sharma, T. Saravanan, R. Reena, R.K. Bhagat, B. Jolad, K.K. Naidu, "Advanced control strategies for multilevel inverters in renewable energy systems: Enhancing power quality and efficiency," E3S Web Conf., **591**, article 01013, pp. 1–11 (2024).
7. Y. Madi, A. Dendouga, D. Aouzellag, "Predictive direct power control of neutral-point clamped converter in wind turbine system with dual three-phase permanent magnet synchronous generator," Rev. Roum. Sci. Techn. – Électrotechn. Et Énerg., **70***, 3,* pp. 319–324 (2025).
8. A. Berboucha, Y. Hamoudi, K. Djermouni, et al., "Fuzzy logic control of two-stage grid-connected photovoltaic system," Alger. J. Signals Syst., **9**, *2*, pp. 91–97 (2024).
9. D. Xu, H. Cen, "A hybrid energy storage strategy based on multivariable fuzzy coordinated control of photovoltaic grid-connected power fluctuations," IET Renew. Power Gener., **15**, *8*, pp. 1826–1835 (2021).
10. M. Shadoul, R. Ahshan, R.S. AlAbri, A. Al-Badi, M. Albadi, M. Jamil, "A comprehensive review on a virtual-synchronous generator: Topologies, control orders and techniques, energy storages, and applications," Energies, **15**, *22*, article 8406 (2022).
11. X. Gao, D. Zhou, A. Anvari-Moghaddam, F. Blaabjerg, "Stability analysis of grid-following and grid-forming converters based on state-space modelling," IEEE Trans. Ind. Appl., **60**, *3*, pp. 4910–4920 (2024).
12. Y. Yu, X. Hu, "Improved control of parallel virtual synchronous generator based on adaptive voltage compensation," Int. J. Dynam. Control, **10**, *2*, pp. 890–901 (2022).
13. Z. Ling, Y. Liu, Z. Wang, J. Yin, "Adaptive inertia and damping of grid-connected inverter with improved VSG control," IET Power Electron., **16**, *16*, pp. 2769–2781 (2023).
14. T. Shi et al., "Research on adaptive optimal control strategy of virtual synchronous generator inertia and damping parameters," IET Power Electron., **17**, *1*, pp. 121–133 (2024).
15. J. Huang, X. Lin, J. Sun, H. Xu, "A stabilization control strategy for wind energy storage microgrid based on improved virtual synchronous generator," Energies, **17**, *11*, article 2567 (2024).
16. F. Liu, Y. Zhao, H. Wang, J. Zhang, L. Zhang, "Adaptive VSG control strategy considering energy storage SOC constraints," Front. Energy Res., **11**, article 1278648 (2023).
17. Y. Daili, A. Harrag, "Improved decoupling virtual synchronous generator control strategy," Rev. Roum. Sci. Techn. – Électrotechn. Et Énerg., **66**, *3*, pp. 153–160 (2021).
18. S. Nacef, R. Babouri, K. Ghedamsi, A. Houari, "Fault-resilient control strategy for cascaded multilevel inverters in grid-connected PV systems," Period. Polytech. Electr. Eng. Comput. Sci., **69**, *2*, pp. 148–158 (2025).
19. K.A. El Wahid Hamza, H. Linda, L. Cherif, "LCL filter design with passive damping for photovoltaic grid-connected systems," IREC – 6th Int. Renew. Energy Congr., Sousse, Tunisia, pp. 1–4 (2015).
20. Y. Huang, D. Wang, L. Shang, G. Zhu, H. Tang, Y. Li, "Modeling and stability analysis of DC-link voltage control in multi-VSCs with integrated to weak grid," IEEE Trans. Energy Convers., **32**, *3*, pp. 1127–1138 (2017).
21. N. Jin, J. Yang, J. Jiang, F. Meng, D. Sun, "Research on double closed-loop control system of NPC cascaded H-bridge photovoltaic inverter," Lect. Notes Electr. Eng., **1160**, pp. 602–614 (2024)